Exploiting the PRISM Feature and Purity Monitors of the SBND Neutrino Detector

Eleonora Ponticelli[1]*, Under the supervision of Ornella Palamara, Marco Del Tutto

Abstract
The **Short-Baseline Neutrino** (**SBN**) **program** at **Fermilab** will pursue neutrino properties searches, exploiting three **Liquid Argon Time Projection Chamber** (**LArTPC**) experiments to investigate ν_e appearance and ν_μ disappearance in the Booster Neutrino Beam (BNB). **SBND** will be the near detector in the program, measuring the un-oscillated flux. It is anticipated to begin operating in 2023. Thanks to its peculiar proximity to the neutrino source of about 110 meters, SBND will collect extremely high statistics data of the flux in the GeV energy range, providing **unprecedented precision measurements**. SBND particular setting also allows to take measurements at different distances from BNB's center maintaining statistics high enough at each range. LArTPC and the cold electronics technologies, as well as the Argon-neutrino interaction studies, will play a key role in future neutrino physics. In this prospect, this work was focused on two SBND features: **SBND PRISM** tool, with the aim of investigating neutrino flux at different distances from the beam axis, and **Purity Monitors**, which provide a clever measurement of Argon purity in the detector, whose value is fundamental in neutrino-Argon interaction.

Keywords
SBN — SBND — Neutrino — LArTPC — SBND PRISM — Purity Monitor

[1] *Dipartimento di Fisica "Ettore Pancini", Università degli Studi di Napoli "Federico II"*
***Author**: eleonora.ponticelli@live.it

Contents

1. The SBN Program

The Short Baseline Neutrino (SBN) program consists in three functionally identical Liquid Argon Time Projection Chamber (LArTPC) detectors located along the Booster Neutrino Beamline (BNB) at the Fermi National Accelerator Laboratory [1]. SBN program's main goals include:

- *Beyond Standard Model searches*, involving the search for eV mass-scale sterile neutrinos

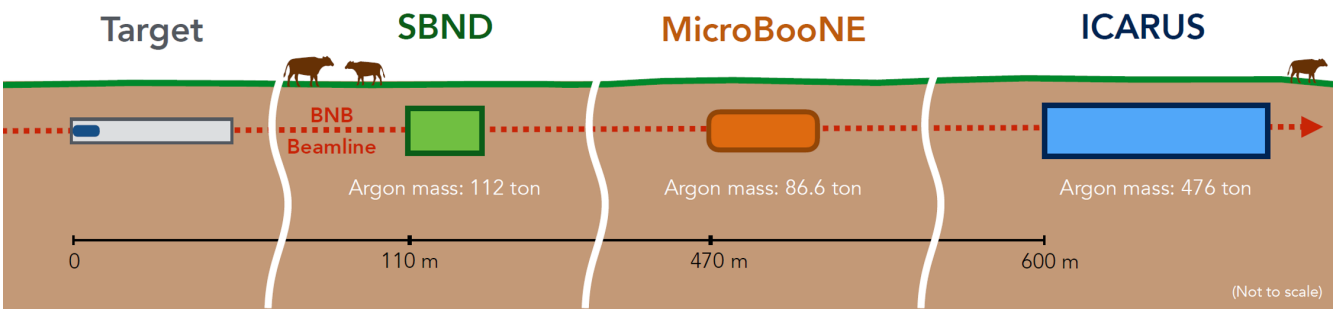

Figure 1. Scheme of the Short-Baseline Neutrino Program detectors set along the Booster Neutrino Beamline.

oscillations and the study of neutrino-Argon interactions at the GeV energy scale.
- *LArTPCs technology improvement*, to be also used in the DUNE/LBNF long-baseline neutrino experiment in the next decade.

A scheme of the SBN program detector placing is shown in Figure 1. Starting from the beam source, the three detectors of SBN are:

- The **Short-Baseline Near Detector** (**SBND**), which is located 110 meters far from the target and has an Argon Mass of 112 tons. SBND is therefore the nearest detector to the source out of the three. This feature guarantees high statistics in measurements, thanks to the small solid angle at which neutrinos enter the detector. In this way, SBND setting provides to greatly reduce systematic uncertainties.

- The **MicroBooNE Detector**, which is a 89-ton LArTPC that is about 470 meters far from the target. MicroBooNE first started collecting neutrino data in October 2015.

- The **ICARUS Detector**, which is set about 600 meters from the target and has a 476 tons active mass. ICARUS was previously set at the Gran Sasso Laboratory in Italy and it was then moved to Fermilab in 2017, where it was upgraded.

1.1 Booster Neutrino Beam (BNB)

SBN program will take place along the Booster Neutrino Beamline (BNB). The beam is produced by extracting 8 GeV kinetic energy protons from Fermilab's Booster accelerator and having them impact on a Beryllium target. Through this interaction, mainly kaons and pions are produced, which later decay into leptons and associated neutrinos. In this way, the neutrino beam is formed and focused towards the detectors. The neutrino flux at the SBND front face is mainly formed by ν_μ, with a smaller percentage of ν_e. Neutrinos relative abundances are shown in Figure 3, along with Neutrino Flux as a function of Neutrino Energy. It is fundamental to notice that electrons neutrinos come from 3-bodies decays, while muon neutrinos come from 2-bodies decays. This implies constrains on events' kinematics and therefore on neutrinos' energy. ν_μ and ν_e most probable source decays are reported in Figure 2.

$$\pi^+ \to \nu_\mu + \mu^+ \qquad \mu^+ \to \nu_e + \bar{\nu}_\mu + e^+$$
$$K^+ \to \nu_\mu + \mu^+ \qquad K^+ \to \nu_e + e^+ + \pi^0$$
$$K_L^0 \to \nu_e + \pi^- + e^+$$

Figure 2. ν_μ and ν_e source decays.

2. SBND

The operation of the three detectors guarantees taking measurements from the same neutrino beam at different distances from the source. SBND will

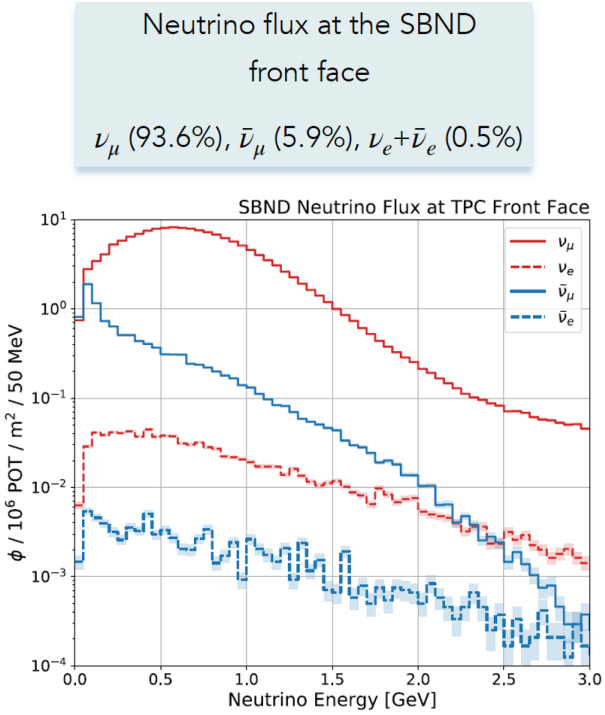

Figure 3. Neutrino Flux at the SBND front face as a function of Neutrino Energy, along with neutrinos' abundance percentage.

measure the unoscillated BNB neutrino flux, collecting extremely high statistics measurement thanks to its proximity to the target. The large data sample will also allow unprecedented high precision cross section measurements in the GeV energy range, in many different electron neutrino and muon neutrino exclusive channels [2].

2.1 LArTPCs

Liquid Argon Time Projection Chambers (LArTPCs) are calorimetric imaging particle detectors. The SBND detector has an active volume of purified liquid Argon of 5.0m (L) x 4.0m (W) x 4.0m (H). It consists of **2 contiguous TPCs** with a **central shared cathode** and **two anodes**, one at each side of the detector. It is all surrounded by a Field Cage. An approximately uniform electric field is so applied to the Argon volume. Neutrinos impact in the TPC and they scatter with Argon nuclei through **charged-current** (**CC**) or **neutral-current** (**NC**) weak interaction. The resulting charged particles both ionize and excite Argon atoms. LAr ionization produces free electrons that drift towards the anode planes. In addition, vacuum ultraviolet (**V-UV**) scintillation light ($\lambda = 128nm$), is emitted in excited Argon de-excitation. Photons are then collected by the Photon Detection System.

Sense Wires Since electric field strengths of about 500 V/cm are applied, electrons drift towards the anode planes, which are composed of **sense wires**. Electrons have slow drift velocities of about $1.6\frac{mm}{\mu s}$, requiring a continuous readout time of $1-2ms$. With the aim of generating multi-dimensional views of particle tracks, three planes of $150\mu m$-diameter copper-beryllium wires are used. Wire planes are spaced of 3 mm one from the other. The first two planes that electrons cross are rotated of ± 60 degrees with respect to the vertical direction. Electrons pass through the first two wire planes, which are biased, inducing bipolar signals. They then arrive on the last wire plane, which is vertical and positively biased, where they are collected producing a unipolar signal. A scheme of the track reconstruction through the TPC functioning is shown in Figure 4.

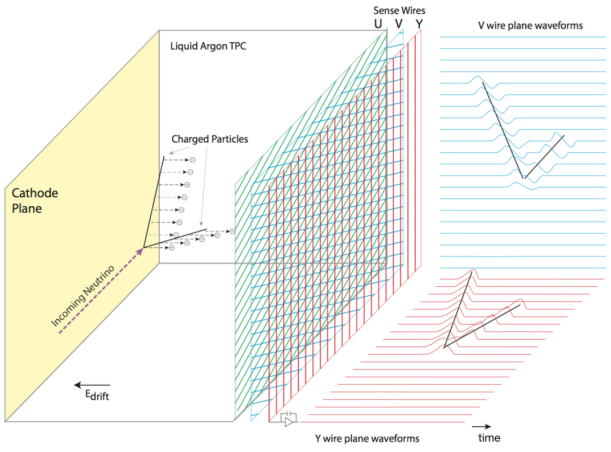

Figure 4. LArTPC track reconstruction working principle, including a view of the waveforms observed on the wires.

Photon Detection System Photons produced in Argon's de-excitation are collected by the Photon Detection System (PDS). The SBND PDS is composed of **active** and **passive elements**.

The *active system* is composed of **120 Hamamatsu PhotoMultiplier Tubes** (**PMTs**). 96 PMTs are coated in tetraphenyl butadiene (**TPB**) in order to detect V-UV photons, for it acts as *wavelength shifter*. 24 PMTs are uncoated instead, to observe visible light directly. Furthermore, the active system comprehends **192 X-ARAPUCAs** as well. X-ARAPUCAs [3] are innovative Silicon PhotoMultipliers (**SiPMs**) topped with *dichroic filter windows* which allow to capture scintillation light with great acceptance. Both V-UV and Visible Light are detected by different types of X-ARAPUCAs. A picture of the active system of SBND's PDS is showed in Figure 5.

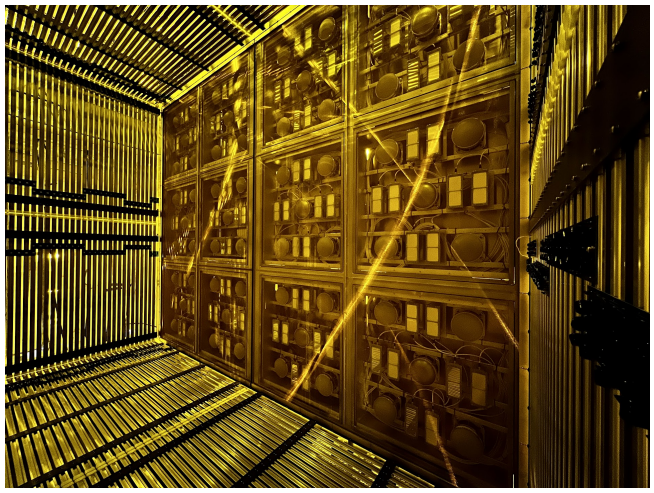

Figure 5. A photo of the light detection system of SBND. Several modules of PMTs and X-ARAPUCAs can be seen. *(Photo: SBND collaboration)*

The *passive* component of SBND PDS consists of **Wavelength-Shifting Reflective Plates** located on the cathode that prevent photon loss as much as possible, redirecting photons towards the active system. SBND PDS has the crucial task of providing the timing of interactions within the LAr volume; therefore, it provides measurements of the position along the drift direction.
Through its features, SBND LArTPC is therefore a high resolution detector that provides **3D imaging** of particle tracks with both **geometrical** and **calorimetrical reconstruction**. A simulation of what a reconstructed track through the TPC operation is shown in Figure 6.

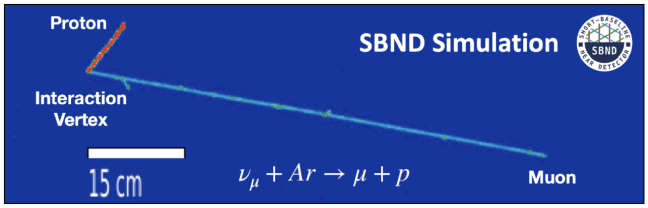

Figure 6. ν_μ event reconstructed through the operation of the TPC.

2.2 Cosmic Ray Tagger

The SBND detector is placed underground, near the Earth's surface. Cosmic Rays impacting the area represent the main component to the background in data analyses. Cosmic rays events can indeed be misidentified as neutrino events, occurring at much higher rates than neutrino interactions. A **Cosmic Ray Tagger** (**CRT**) system was developed to identify the external cosmic interaction [4]. The CRT system is composed of individual scintillator modules readout by SiPMs. Timing of CRT signals is compared to timing of beam events, so that cosmic rays can be identified as such. However, it is not possible to distinguish all in-going cosmic muons from outgoing neutrino-produced muons. Software methods of background removal are to be used along with the CRT system to minimize misidentification [5].

2.3 SBND off-axis setting

The SBND detector has the peculiarity that the central axis of the detector does not coincide with the central axis of the beamline, as shown in Figure 7. The shift between the beamline and the TPC's central axis guarantees that the beamline impacts the detector on his active region. If the two axes were aligned, it would in fact impact the central cathode.

In Figure 7 it is evident that neutrino enter the TPC at **several solid angles**. In terms of distance from the beamline, several **Off-Axis Angles** (**OAAs**) can be identified. It is so possible to think of slicing the detector in **Off-Axis Angle Areas** as shown in Figure 8.

In this way, one can sample the flux in the several OAA regions and study dependency of measurements as a function of the OAA. In these terms,

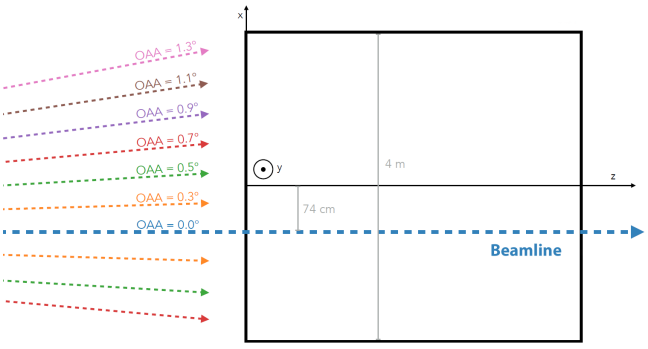

Figure 7. View from the top of the SBND detector. SBND sees neutrinos from several Off-Axis Angles (OAAs). The z-axis, representing the central axis of the detector, is shift with respect to the beamline.

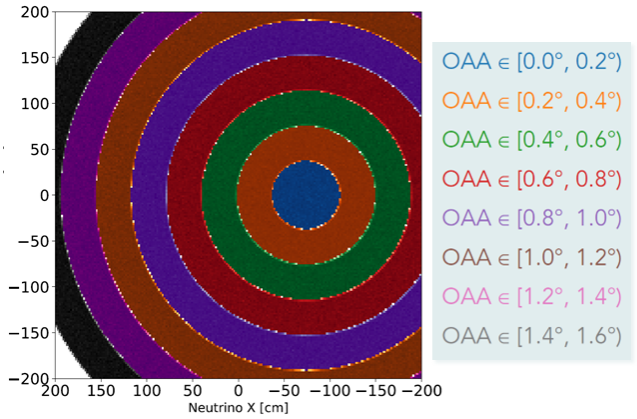

Figure 8. 2-D representation of the Off-Axis Angle Regions [6].

the shifted beamline configuration gives SBND a *unique feature*. In fact, one can explore outer OAA regions that would not be explored otherwise without the shift. This is clearly pointed out in Figure 7; as an example, regions of $OAA = 1.1°, 1.3°$ could not be studied otherwise. Doing so is important for reasons that will be stated later on.

3. SBND PRISM

The acronym **PRISM** stands for **Precision Reaction Independent Spectrum Measurement** and it represents the feature of analyzing measurements at different OAAs. PRISM provides SBND the unique feature of **sampling multiple Off-Axis fluxes with the same detector**. The neutrino flux was so studied in each of the OAA regions, considering neutrinos' energy and associated leptons' momentum and scattering angles. OAA regions were sliced with a 0.2° step.

3.1 SBND PRISM for Neutrinos

The study revealed that neutrino energy distributions are affected by the off-axis position, as shown in Figures 9 & 10. The study was led both for muon neutrinos and electron neutrinos.

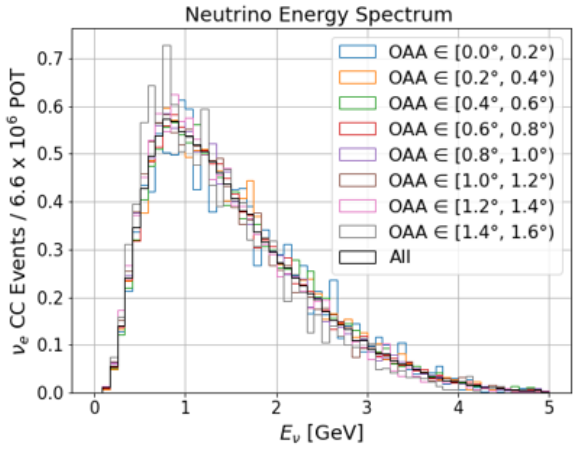

Figure 9. ν_e Energy Distribution for several OAA values.

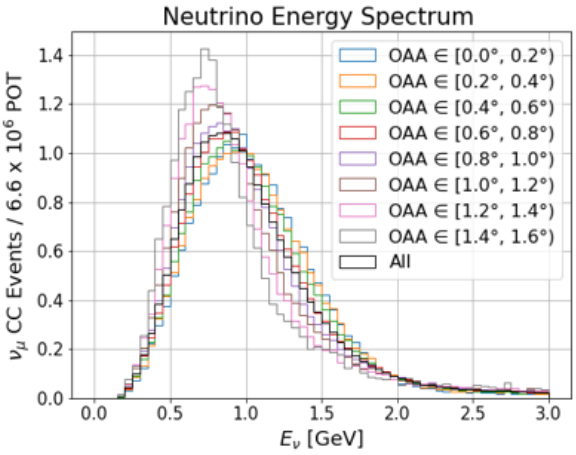

Figure 10. ν_μ Energy Distribution for several OAA values.

Data was normalized to the value of 6.6×10^{20} **protons on target**, which was calculated to correspond to ~ 3 years of operation [7].

It is noticeable that neutrinos of both flavors exhibit the same behavior as a function of the OAA position. Indeed, **the expected values of the distributions take smaller values by going more off-axis**. This means that the more one goes off-axis, the smaller the neutrino energy is, as expected. Moreover, by going farther off-axis, distributions tighten for smaller uncertainty values. This means that measurements are more precise if taken farther off-axis. In this respect, PRISM reveals itself to be a useful tool. This behavior is evident for both flavors, even though it is more evident for muon neutrinos. Since muon and electron neutrinos respectively come from two- and three-bodies decays, they have strictly different kinematics. This can be an explanation to the wider separation of distributions when it comes to muon neutrinos. ν_e to ν_μ ratios were then studied at fixed energy. Resulting plots are shown in Figure 11.

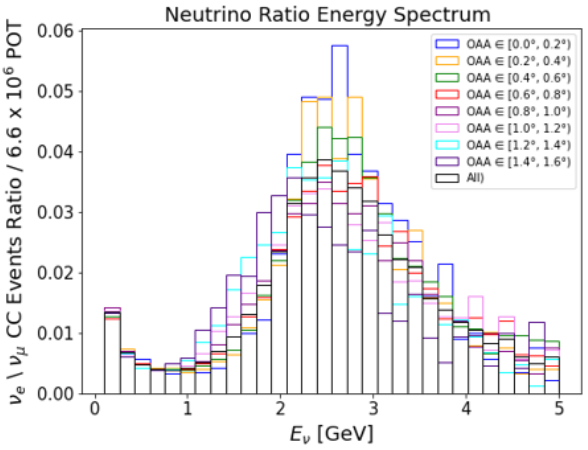

Figure 11. ν_e to ν_μ Ratio Energy Distribution for several OAA values.

As expected, ratios exhibit the same behavior of single flavor histograms. The same plot was explicated only for the most on-axis angle and the most off-axis one, to show the difference in the off-axis region more clearly (Figure 12).

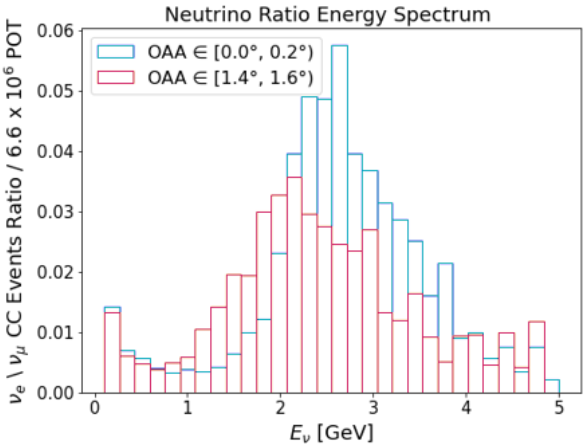

Figure 12. ν_e to ν_μ Ratio Energy Distribution for the most on-axis angle and the most off-axis one.

3.2 MicroBoone data and GENIE simulation

Measurements taken in the *MicroBoone collaboration* explicated **discrepancies** with respect to simulated data through **GENIE** when it comes to leptons parameters [8] [9]. Both muon momentum and cosine of scattering angle showed this behavior in terms of cross section. In particular, the higher the value of these parameters, the greater the discrepancies, as shown in Figures 13 & 14.

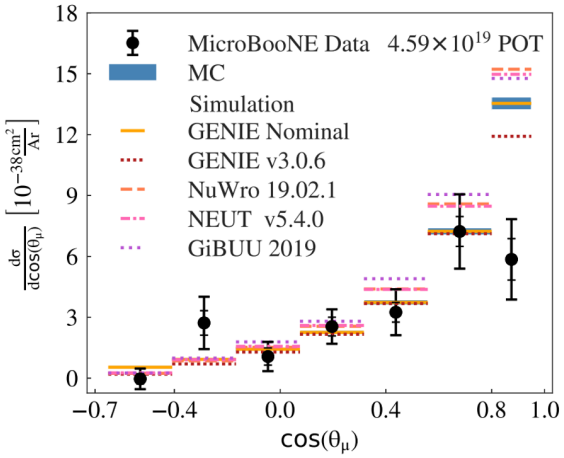

Figure 13. Flux-integrated single differential ν_μ cross sections as a function of the cosine of muon scattering angle. The data (black) is compared to the default GENIE prediction [8].

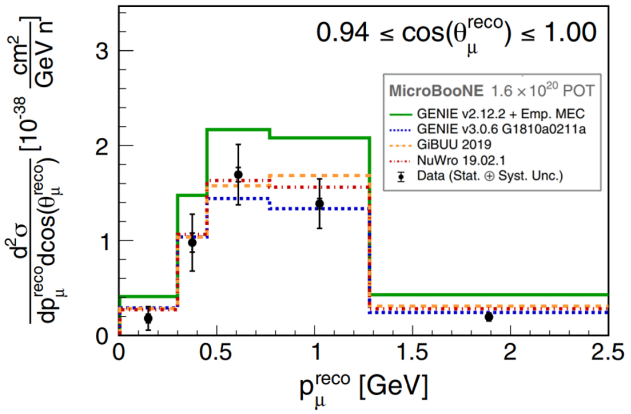

Figure 14. ν_μ inclusive double-differential cross section on Argon per nucleon as a function of the reconstructed muon momentum. The data (black) is compared to the default GENIE prediction [9].

Ranges around high values have not been actually explored by the MicroBoone collaboration, for they correspond to too high values of leptons energy for the detector to collect. It is therefore relevant to study these ranges in order to better understand the behavior of leptons' momentum and scattering angles at high energies.

3.3 SBND PRISM for Leptons

For the reasons stated above, **leptons momentum distributions** were studied. Once again, data was normalized to 6.6×10^{20} protons on target. Distributions are shown in Figures 15 & 16. Simulation provided enough data for each OAA region to have relevant statistics, as SBND will collect high number of data for its proximity to the target. To prove this, the number of events for each OAA region in plots 15 & 16 was transcribed in Table 1. Table 1 is also valid for Figures 9 & 10 , as every ν_μ event corresponds to an associated μ event.

Leptons spectra in terms of different off-axis angles explicated the same behavior as the neutrino ones. Once again, the behavior pops out strongly on the tails and spectra are more separated for muons. To point out behaviors in terms of OAAs, plots only showing the most-on-axis distribution and the most-off-axis one are displayed in Figures 17 & 18.

e to μ ratios were studied at fixed lepton kinetic energy. Figure 3.3 exhibits the resulting plot for the most on-axis angle and the most off-axis one.

OAA index	N ν_μ events	N ν_e events
1	155840	1004
2	454059	3075
3	711735	4910
4	753539	5390
5	740447	5469
6	422513	3294
7	286149	2340
8	74061	625
All	3599107	26119

Table 1. Number of events for each OAA region for Electrons and Muons Momentum Distributions in Figures 15 & 16.

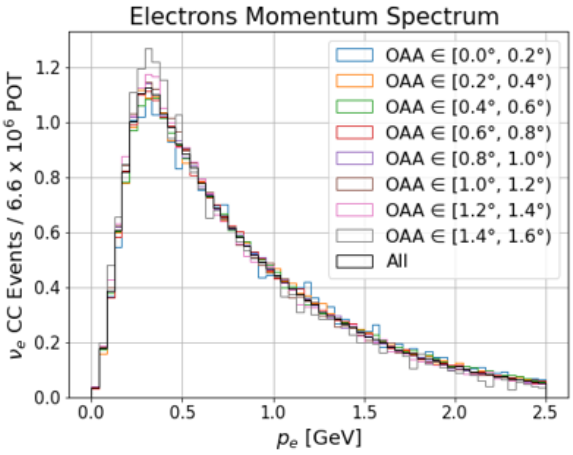

Figure 15. Electrons Momentum Distribution for several OAA values.

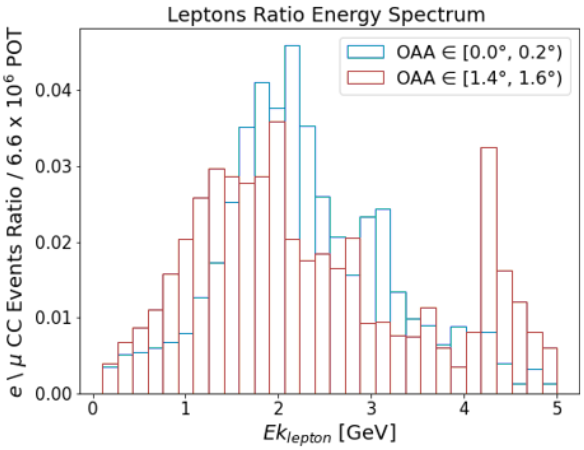

Figure 19. e to μ Ratio Energy Distribution for the most on-axis angle (in blue) and the most off-axis one (in red)

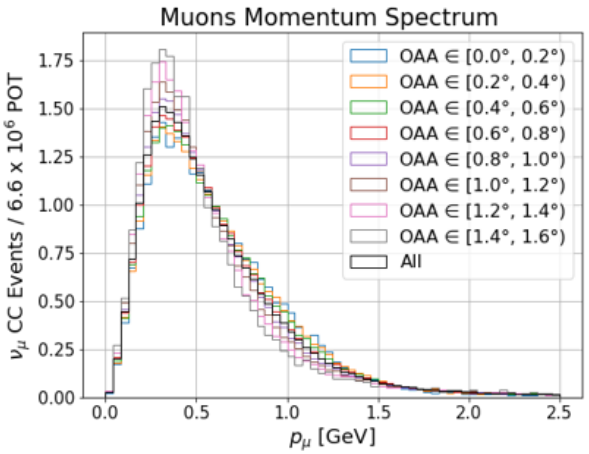

Figure 16. Muons Momentum Distribution for several OAA values.

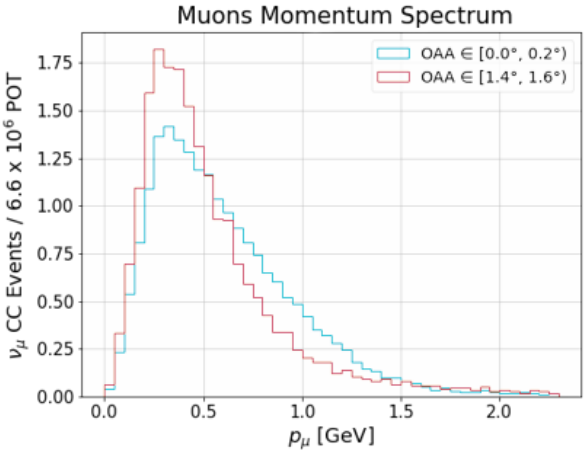

Figure 18. Muon Momentum Distribution for the most on-axis angle (in blue) and the most off-axis one (in red).

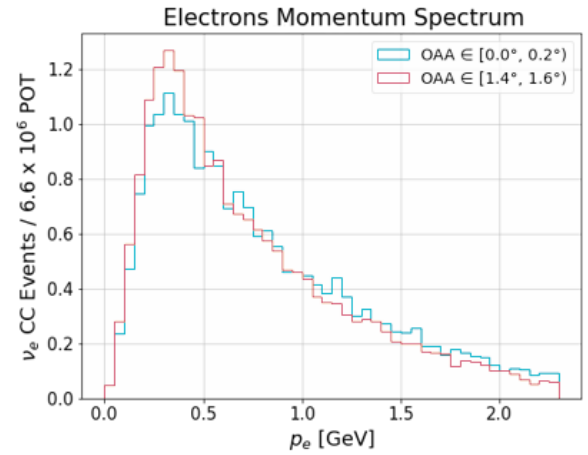

Figure 17. Electrons Momentum Distribution for the most on-axis angle (in blue) and the most off-axis one (in red).

SBND PRISM for Muons The study was focused only on muons for the reasons stated before. Muon momentum distributions in terms of cosine of scattering angles were investigated. Resulting spectra are reported in Figure 20 , that shows once more the most-on-axis distribution and the most-off-axis one.

Along with increasing values of cosine of scattering angles, the most probable values of distributions shifts significantly to higher momentum values. Furthermore, **distributions at different OAA become more distinguished at higher scattering angles**. Exploiting the PRISM feature in this range allows to significantly distinguish between different OAAs measurements. **In this range, distributions tighten for smaller uncertainty values, resulting in greater measurement sensitivity. PRISM can be therefore used to take more precise measurements just by analyzing them more off-axis.** It is fundamental to point out that higher cosine of scattering angles correspond to leptons going more forward with respect to the beam direction. **This means that PRISM feature can be a key tool to study forward highly energetic leptons.** In this respect, the investigated cosine of scattering angle was restricted to the $0.95 < \cos\theta_\mu < 1$ range. Resulting distributions are shown in Figure 21, where the discussed behavior is explicated.

3.4 Conclusions on PRISM

To recap, with leptons going more forward, there's a relevant distinction between momentum distributions at different OAAs. This means that measurements sensitivity grows in this region, which would remain unexplored without PRISM. Slicing in OAAs is important to understand this behavior, which is strictly linked to physics. Measurements in a farther OAA slice show tighter distributions and have therefore smaller uncertainties. This leads to more precise measurements just going more off-axis. In this scenario, PRISM reveals itself to be crucial tool: not only SBND will provide unprece-

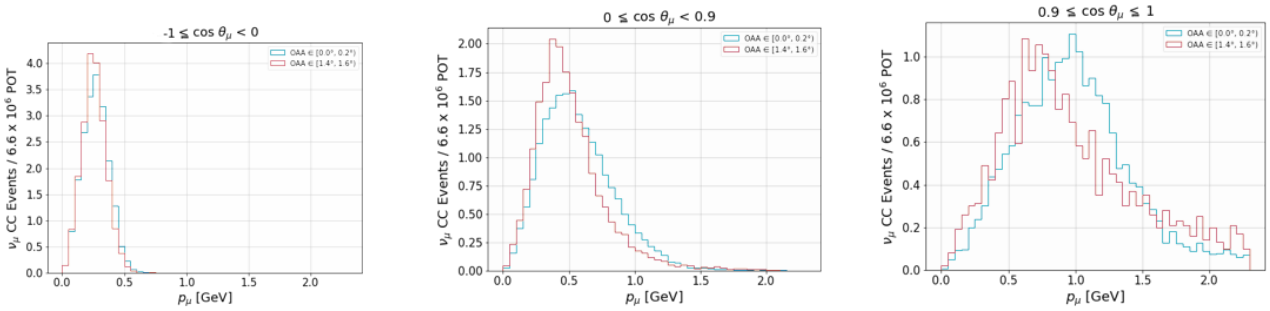

Figure 20. Muon Momentum Distributions for the most on-axis angle (in blue) and the most off-axis one (in red) for several cosine of scattering angle values ranges.

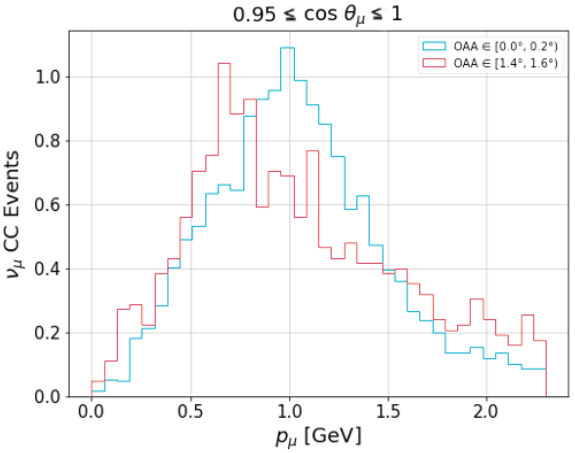

Figure 21. Muon Momentum Distribution for the most on-axis angle (in blue) and the most off-axis one (in red). Values of the cosine of the scattering angle were restricted to the range between 0.95 and 1.

dented precision measurements thanks to its close setting to the target, but the use of PRISM will ensure to **further reduce uncertainties simply by sampling fluxes far off-axis**.

4. Purity Monitors

While drifting through sense wires, electrons can be captured by LAr positively-charged *impurities*. This results in loss in terms of output signal. To avoid that, it is fundamental to verify that LAr is as pure as possible. In this respect, **Purity Monitors** (**PrM**) are used to check LAr purity through electrons' drifting time measurements [10]. SBND will count 3 Purity Monitors of different lengths to guarantee Argon purity.

Purity Monitors are **double-gridded ion chambers**. They are composed of four circular electrodes, all parallel to each other, as reported in Figure 22:

- a **Photocathode**,
- two open wire **Grids**, acting as **Cathode** and **Anode** respectively,
- an **Anode**.

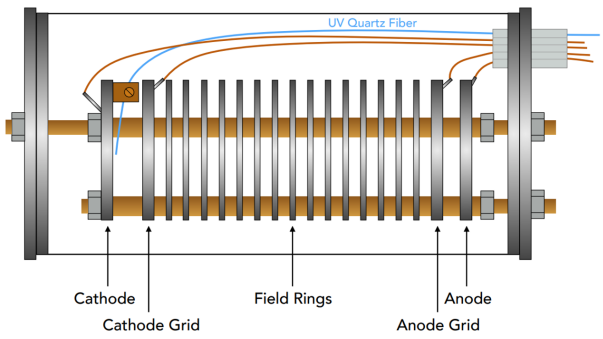

Figure 22. Scheme of a Purity Monitor.

4.1 Purity Monitors working principle

Electrons freed from the Photocathode drift towards the Cathode Grid, inducing current as passing through. Once the Cathode Grid current is amplified and integrated, it actually provides a measurement of the charge emitted by the Photocathode. This represents an estimation of charge before any electron has recombined with LAr impurities. Electrons then drift across the PrM and some of them get captured

by LAr impurities. The remaining electrons pass through the Anode Grid and impact then on the Anode, providing a second measurement in terms of charge [11]. Charge collected on the Cathode Grid (Q_C) and on the Anode (Q_A) can be so used to estimate the electron lifetime τ as shown in Equation 1, where t_{drift} is the drifting time of electrons across the PrM.

$$Q_A = Q_C \times e^{-\frac{t_{drift}}{\tau}} \quad (1)$$

4.2 Experimental Setup

A scheme of the employed experimental setup is shown in Figure 23. Electrons are freed from the Photocathode by using a **Flash Lamp** emitting in the UV spectrum, that also provides trigger timing to the **DAQ Computer**. The DAQ Computer pilots the flash lamp through an **Automation Module** and photons are sent to the Purity Monitor through **optical quartz fibers**. One positive and one negative **High Voltage** (**HV**) **Power Supplies** are controlled by the DAQ Computer and send HV to the PrM, passing through **Electronics Modules**. These modules also pick up Cathode and Anode signals from the PrM and send it to the DAQ Computer.

4.3 Measurements

The exploited Purity Monitor's specifications are reported in Table 2.

Characteristic	Value
Cathode, Anode disk, grid diameter	8 cm
Cathode-Cathode Grid gap	1.8 cm
Anode Grid-Anode gap	0.79 cm
Anode disk/Cathode disk thickness	0.23 cm
Anode grid/Cathode grid thickness	0.24 cm
Field-shaping ring thickness	0.23 cm
Gap between rings	0.79 cm
Cathode-Anode total drift distance	50 cm
Cathode grid to Anode grid distance	47 cm
Number of field-shaping rings	45
Number of resistors	46
Nominal Cathode Voltage	-100 V
Nominal Anode Voltage	5 kV

Table 2. Purity Monitor specifications.

A graphic interface was specially developed to study the resulting Cathode Grid and Anode signals over sampling time. The study focused on measurements in gaseous Argon (GAr) , with the goal of confronting in-vacuum, in-GAr and in-LAr measurements. Many runs with different applied voltages were performed. **Run n.11** is shown in Figure 24 as an examples of the resulting signals. In Table 3, the applied voltages for Run n.11 are reported.

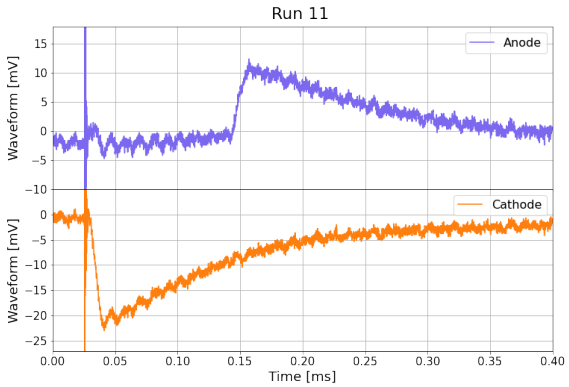

Figure 24. Resulting Cathode and Anode Signals for Run 11.

Electrode	Voltage Value (V)
Cathode	-100
Cathode Grid	0 (Ground)
Anode Grid	2700
Anode	3000

Table 3. Applied voltage to electrodes for **Run 11**.

It is noticeable that waveforms look as expected. The amplitude of the Anode signal is about 10 mV; the spike at $t \sim 0.025ms$ is caused by flash lamp noise.

Cathode, Cathode grid and Anode voltages were set to the fixed values in Table 3, while Anode Grid voltage was increased with a 100V step. The step was enlarged by going towards the Anode Voltage values, performing several runs.

Anode Grid Voltage was then tested at critical values with respect to Anode Voltage. Anode Grid

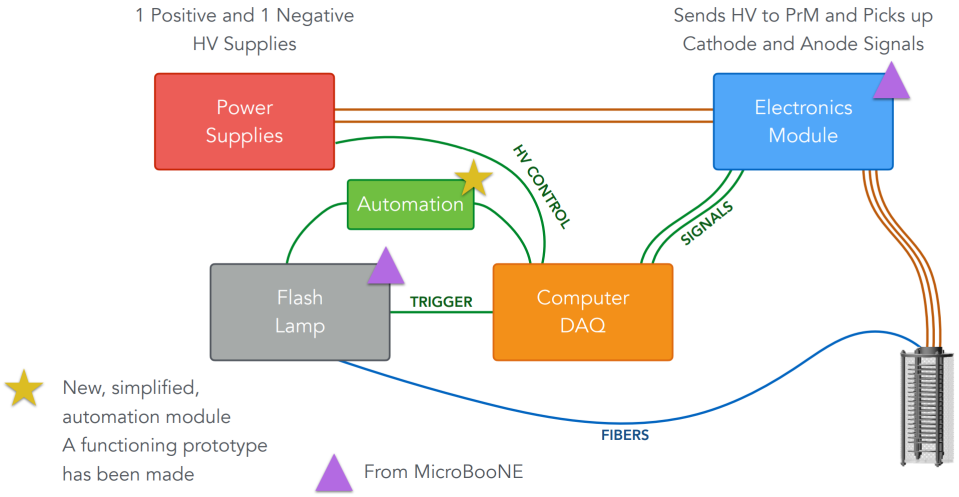

Figure 23. Electronics Setup for Purity Monitor characterization.

Voltage was set at the same value as Anode Voltage and over, as shown in Figure 25. Set voltages are reported in Table 4 for the shown runs.

Run Number	V Anode Grid (V)	V Anode (V)
23	3000	3000
25	3175	3000
27	3200	3000

Table 4. Applied voltage to electrodes for **Run 23**, **25** , **27**.

It is evident that Anode Signal does not drop to zero when the electrodes have the same voltage values. Anode Signal reduces to half of his value only when Anode Grid Voltage exceedes 150V over the critical value, dropping to zero towards 200V over threshold.

4.4 Conclusions on Purity Monitors

A reasonable interpretation of the results is that the electric field is not strong enough to instantly stop electrons or to instantly attract them back once they have passed the Anode Grid. Since the electrons arrive on the grid with a non-zero momentum, they keep on going forward and they are collected on the Anode anyway. It is in fact only when the Anode Grid voltage exceedes the Anode one of about **200V** that no signal is observed on the anode. Further studies about this behavior are to be led to figure out proper values of applied voltage. This will allow to characterize Purity Monitors for what concerns *transparency*, which is a fundamental feature in terms of gain.

Acknowledgments

I would like to express my gratitude to my supervisors, Ornella Palamara and Marco Del Tutto, for guiding me through this experience of both professional and personal growth. Thanks to them, I have acquired practical scientific skill and learned how to overcome the pressure of hard work that characterizes scientific research. In this prospect, I also have to express my gratitude to the members of the SBND collaboration that assisted me, in particular to Vishvas Pandey.

I am also extremely grateful to the organizing committee of the Italian Summer Student Program at Fermilab, Simone Donati, Giorgio Bellettini, Emanuela Barzi and Marco Mambelli, for selecting me and giving me this unique, important formative opportunity.

Lastly, I want to thank my fellow interns Giulia Liberalato, Riccardo Triozzi, Vanessa Cerrone and Clara Saia, whom I could count on for anything from the first to the last moment of this experience and beyond.

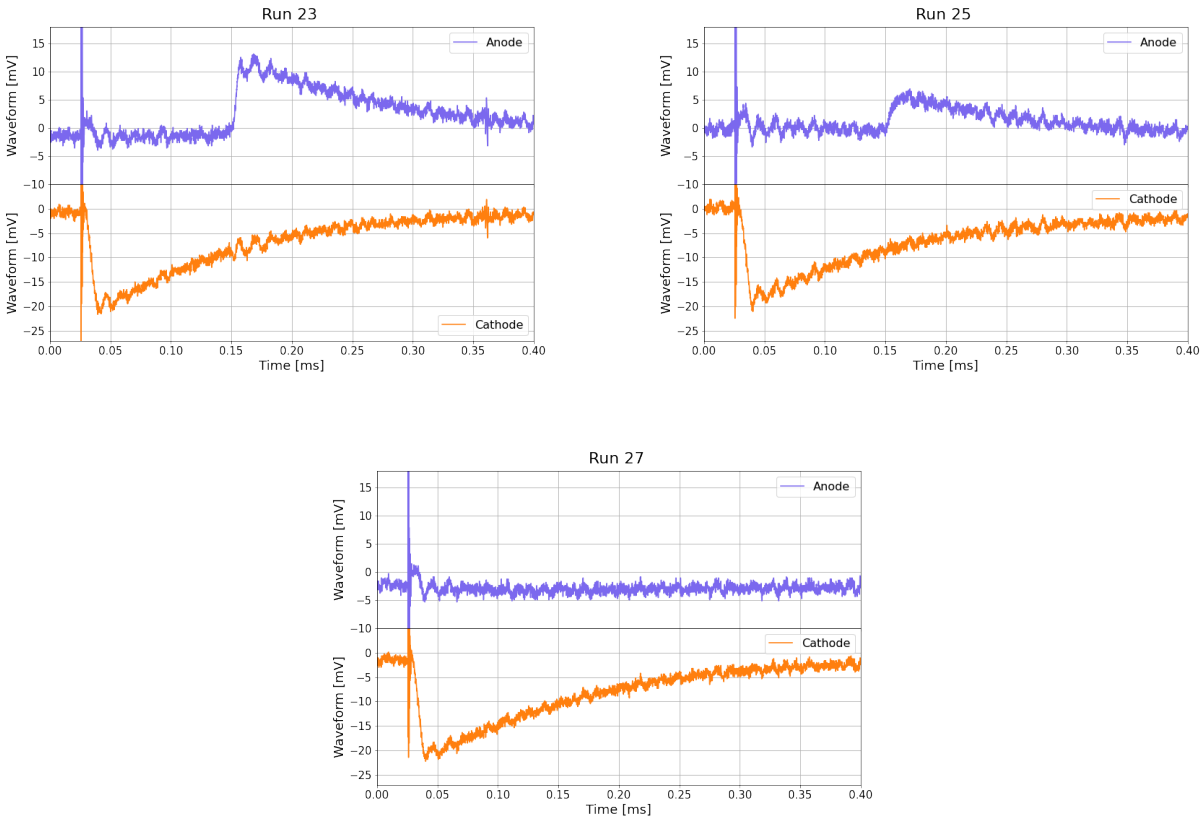

Figure 25. Resulting Anode and Cathode signals by increasing Anode Grid voltage.

References

[1] Pedro A.N. Machado, Ornella Palamara, and David W. Schmitz. The short-baseline neutrino program at fermilab. *Annual Review of Nuclear and Particle Science*, 69(1):363–387, 2019.

[2] Varuna Meddage. Status of the Short-Baseline Near Detector at Fermilab. *PoS*, PANIC2021:273, 2022.

[3] A.A. Machado, E. Segreto, D. Warner, A. Fauth, B. Gelli, R. Máximo, A. Pissolatti, L. Paulucci, and F. Marinho. The x-arapuca: an improvement of the arapuca device. *Journal of Instrumentation*, 13(04):C04026, apr 2018.

[4] M. Auger, M. Del Tutto, A. Ereditato, B. Fleming, D. Goeldi, E. Gramellini, R. Guenette, W. Ketchum, I. Kreslo, A. Laube, D. Lorca, M. Luethi, C. Rudolf von Rohr, J. R. Sinclair, S. R. Soleti, and M. Weber. A novel cosmic ray tagger system for liquid argon tpc neutrino detectors, 2016.

[5] SBND Collaboration, R. Acciarri, C. Adams, C. Backhouse, William Badgett, L. Bagby, V. Basque, Maria Cecilia Bazetto, A. Bhanderi, A. Bhat, D. Brailsford, G. Brandt, F. Carneiro, Y. Chen, Hungwei Chen, G. Chisnall, I. Crespo-Anadón, E. Cristaldo, Clara Cuesta, and A. Zglam. Cosmic background removal with deep neural networks in sbnd. 12 2020.

[6] Marco Del Tutto, Pedro A. N. Machado, Kevin James Kelly, and Roni Harnik. SBND-PRISM: Sampling Multiple Off-Axis Fluxes with the Same Detector. 2021.

[7] J.I. Crespo-Anadón. Status of the short-baseline near detector at fermilab. *Journal of Physics: Conference Series*, 2156(1):012148, dec 2021.

[8] P. Abratenko, M. Alrashed, R. An, J. Anthony, J. Asaadi, A. Ashkenazi, S. Balasubramanian, B. Baller, C. Barnes, G. Barr, V. Basque, L. Bathe-Peters, O. Benevides Rodrigues, S. Berkman, A. Bhanderi, A. Bhat, M. Bishai, A. Blake, T. Bolton, L. Camilleri, D. Caratelli, I. Caro Terrazas, R. Castillo Fernandez, F. Cavanna, G. Cerati, Y. Chen, E. Church, and D. Cianci et al. First measurement of differential charged current quasielastic-like ν_μ-argon scattering cross sections with the MicroBooNE detector. *Physical Review Letters*, 125(20), nov 2020.

[9] Marco Del Tutto. *First Measurements of Inclusive Muon Neutrino Charged Current Differential Cross Sections on Argon at 0.8 GeV Average Neutrino Energy with the MicroBooNE Detector*. PhD thesis, Oxford U., 2019.

[10] Measurement of the Electronegative Contaminants and Drift Electron Lifetime in the MicroBooNE Experiment. 5 2016.

[11] Tingjun Yang. Calibration of calorimetric measurement in a liquid argon time projection chamber. *Instruments*, 5:2, 12 2020.